Fine-scale invariants in turbulence generated by rising bubbles

By I. Paul and M. S. Dodd

1. Motivation and objectives

Turbulent flows contain large- and small-scale eddies, where the non-linear interaction between the eddies causes the energy cascade. At the end of the cascade, the energy is dissipated at smaller eddies as the viscosity becomes important (Richardson 1926; Kolmogorov 1941). Studies on turbulent flows, with their main focus on transport processes, consider the large scales because they contain most of the turbulent kinetic energy used for transporting mass, momentum, and heat. On the other hand, analysis of small scales in turbulent flows helps us to construct theories of turbulence given that they tend to show universal characteristics (Sreenivasan & Antonia 1997).

We are interested in the fine-scale structure of turbulence in this work. It is established in the literature that the following characteristics of small-scale turbulence are universal in homogeneous isotropic turbulence (HIT). They are: (i) topology of the flow, (ii) vortex stretching and compression, (iii) self-production of strain, and (iv) geometrical alignments. In this study, we are concerned with the topology of the bubbly flow.

It is well-known that any quantity that characterizes topology of a flow should be independent of the coordinate system. This very constraint makes the invariants of different turbulent small-scale tensors ideal for studying the internal coherence of the flow. Particularly, the invariants of the velocity-gradient, rotation-rate, and strain-rate tensors are widely used in the literature to understand the topology, geometry, and dynamics of the turbulent flow. Moreover, information about the small scales would help other turbulent models such as large-eddy simulation (LES) for bubbly flows.

We can write the velocity gradient tensor (VGT) $A_{ij}=\partial u_i/\partial x_j$ (where, $u_i, i=1,2,3$ are the fluctuating velocity components) in terms of its symmetric and antisymmetric parts. We call the symmetric part as the strain-rate tensor, S_{ij} , and the antisymmetric part as the rotation-rate tensor, Ω_{ij} . Here, we can also write the rotation-rate tensor in terms of vorticity components, ω_k , as $\Omega_{ij}=-(1/2)\epsilon_{ijk}\omega_k$, where ϵ_{ijk} is the permutation symbol. The characteristic equation of the VGT is

$$\Lambda_i^3 + P\Lambda_i^2 + Q\Lambda_i + R = 0, \tag{1.1}$$

where Λ_i (i = 1, 2, 3) are the eigenvalues of the VGT. P, Q, R are the first, second, and third invariants of the VGT, respectively. For an incompressible flow, the first invariant of the VGT is zero (P = 0). The second and third invariants of the VGT are given as

$$Q = \frac{1}{4}(\omega_i \omega_i - 2S_{ij}S_{ij}), \tag{1.2}$$

$$R = -\frac{1}{3}(S_{ij}S_{jk}S_{ki} + \frac{3}{4}\omega_i\omega_jS_{ij}). \tag{1.3}$$

The discriminant of Eq. (1.1) is

$$D = \frac{27}{4}R^2 + Q^3. (1.4)$$

Having obtained the invariants of the VGT, we can get the invariants of the strain-rate tensor by setting $\omega_i = 0$ in Eqs. (1.2) and (1.3). Therefore, the invariants of S_{ij} are

$$Q_s = -\frac{1}{2} S_{ij} S_{ij}, (1.5)$$

$$R_s = -\frac{1}{3} S_{ij} S_{jk} S_{ki}. {1.6}$$

Finally, we can get the single invariant of the rotation-rate tensor by putting $S_{ij} = 0$ in Eq. (1.2), and it is

$$Q_w = \frac{1}{4}\omega_i\omega_i. \tag{1.7}$$

The main purpose of these invariants is to reveal information regarding the local topology of the flow field. They have been studied extensively for various turbulent flows and were found to exhibit some universal characteristics (Chong *et al.* 1990; Blackburn *et al.* 1996; Ooi *et al.* 1999; Gomes-Fernandes *et al.* 2014; Meneveau 2011).

The motivation to carry out this current work comes from two facts. First, the aforementioned universal characteristics related to flow coherence have been extensively tested in various standard turbulent cases such as wake, boundary layers, and mixing layers (Blackburn et al. 1996; Ooi et al. 1999; Gomes-Fernandes et al. 2014; Meneveau 2011). However, no such study is available for the bubbly flows. Second, the experiment of Riboux et al. (2010) reports a -3 slope in the turbulent kinetic energy spectrum. This observation is interesting, and VGT dynamics are never studied for flows that exhibit power-law behavior other than the classical -5/3 slope. Since bubbly flows have -3 slope in their spectra, we are interested in looking at their small-scale dynamics as to whether they are similar to or different from the one reported for the HIT. Therefore, this work has two objectives: to document the validation of the direct numerical simulation (DNS) solver for simulating air bubbles rising in water, and to report the similarities and differences in small-scale turbulent invariants between the HIT and bubbly turbulence.

The remainder of this report is organized as follows: The next Section presents the details of the DNS solver. Then, we validate the DNS solver for two cases related to bubbly flows in Section 3. After the validation of the solver, we study the invariants of various tensors related to small-scale turbulence and compare the results against the HIT in Section 4. Finally, we summarize the main conclusions from this work in Section 5.

2. Mathematical formulation and numerical method

2.1. Governing equations

The governing equations for an incompressible flow of two immiscible fluids are

$$\nabla \cdot \mathbf{u} = 0, \tag{2.1a}$$

$$\frac{\partial \mathbf{u}}{\partial t} + \nabla \cdot (\mathbf{u} \otimes \mathbf{u}) = \frac{1}{\rho} \left[-\nabla p + \nabla \cdot (2\mu S) + \mathbf{f}_{\sigma} \right] + \mathbf{g}, \tag{2.1b}$$

where $\mathbf{u} = \mathbf{u}(\mathbf{x}, t)$ is the fluid velocity, $p = p(\mathbf{x}, t)$ is the pressure, $\rho = \rho(\mathbf{x}, t)$ is the density, $\mu = \mu(\mathbf{x}, t)$ is the dynamic viscosity, $S = S(\mathbf{x}, t)$ is the strain-rate tensor $(S = [\nabla \mathbf{u} + \nabla \mathbf{u} + \nabla \mathbf{u}])$

 $(\nabla \mathbf{u})^T]/2$), \mathbf{f}_{σ} is the force due to surface tension, and \mathbf{g} is the gravitational acceleration. The subscripts l and g indicate the liquid and gas phases, respectively. $\mathbf{f}_{\sigma} = \mathbf{f}_{\sigma}(\mathbf{x}, t)$ is the force per unit volume due to surface tension,

$$\mathbf{f}_{\sigma} = \sigma \kappa \delta(s) \mathbf{n},\tag{2.2}$$

where σ is the surface tension coefficient, $\kappa = \kappa(\mathbf{x}, t)$ is the curvature of the bubble interface, $\mathbf{n} = \mathbf{n}(\mathbf{x}, t)$ is the unit vector that is normal to the interface and directed toward the interior of the bubble, δ is the Dirac δ -function that is needed to impose \mathbf{f}_{σ} only at the interface position, and s is a normal coordinate centered at the interface, such that s = 0 at the interface.

2.2. Numerical method

We solve the governing Eqs. (2.1a) and (2.1b) throughout the whole computational domain, including the interior of the bubbles. The governing equations are discretized in space in a Eulerian framework using the second-order central difference scheme on a uniform staggered mesh. The equations are advanced in time using a pressure-correction method, which uses the second-order Adams-Bashforth scheme. The interface is captured in time using the volume of fluid (VoF) method, which determines the sharp interface between the two immiscible fluids using the VoF color function, C, which represents the volume fraction of the gas in each computational cell. The full details, including verification and validation cases, of the VoF and the pressure correction scheme employed can be found in Baraldi $et\ al.\ (2014)$ and Dodd & Ferrante (2014), respectively.

3. Validation of the solver

We first present the validation results for the solver. We apply our solver to two types of problems. The first one is a single bubble rising in quiescent water, and we compare our results with a previously reported simulation. Then, we consider the current problem of an ensemble of air bubbles rising in water leading to bubble-induced homogeneous turbulence. For this case, we compute the energy spectra and probability density functions (PDFs), and compare them against the experimental result.

3.1. Rising bubble validation

To validate the numerical method presented in Section 2.2, we simulate an air bubble rising in quiescent water. The non-dimensional parameters and computational domain size are selected to match a DNS simulation performed by Cano-Lozano et al. (2016). We chose case 3 from their paper for the comparison because it is the only case that both uses water as the liquid and plots the bubble Reynolds number as a function of time. It also yields a bubble diameter of D = 1.64 mm, which is close to the initial bubble diameter used in our subsequent turbulent simulations (D=2 mm), and it allows us to validate the terminal rise velocity against an experimental value (Houghton et al. 1957). The nondimensional parameters are $Mo = 1.11 \times 10^{-11}$, Bo = 0.36, and Ga = 255.28, which are the Morton $(Mo = g\mu^4/\rho\sigma^3)$, Bond $(Bo = \rho gD^2/\sigma)$, and Galilei $(Ga = \rho g^{1/2}D^{3/2}/\mu)$ numbers, where ρ and μ are of the liquid phase. In this regime, the bubble's path is known to be chaotic, and the wake consists of aperiodic shedding of two counter-rotating vortices. Eventually, the bubble reaches a quasi-steady terminal velocity marked by a nearly constant bubble Reynolds number. The computational domain is $8D \times 8D$ in the horizontal plane 32D in the direction aligned with gravity. Periodic boundary conditions are applied in the two horizontal directions and no-slip wall boundary condition is applied

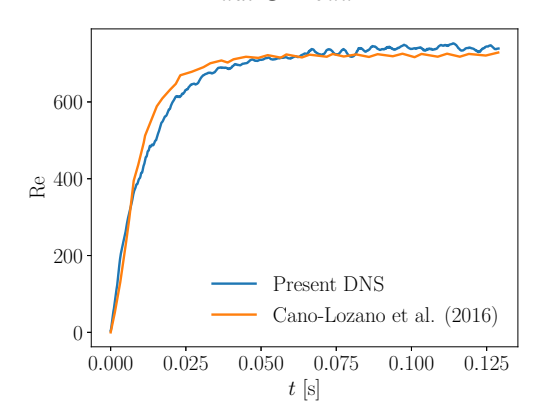


FIGURE 1. Temporal evolution of the Reynolds number of an air bubble rising in quiescent water. Comparison of the present DNS to the numerical result of Cano-Lozano et al. (2016).

at the top and bottom boundaries. The domain is discretized in space on a $90 \times 90 \times 360$ point uniform mesh, giving a bubble resolution of roughly 13 grid points per diameter, which is the same resolution that we use in the turbulent case.

Figure 1 shows the time evolution of the bubble Reynolds number, comparing the current DNS simulation and the numerical result from the literature (Cano-Lozano et al. 2016). The agreement between the two results is good for both the transient phase and the final quasi-steady period. The onset of bubble oscillations at Re = 450 (Clift et al. 2005) is also well captured by the present numerical scheme as indicated by oscillations for Re > 450 (t > 0.01). Note that the results of Cano-Lozano et al. (2016) used mesh refinement near the bubble interface to yield a grid resolution equivalent of 128 computational cells per diameter compared to 13 magnitude larger than used in the present study.

The terminal rise velocity of the bubble is $U_{T,\mathrm{DNS}} = 32.5$ cm/s, which is within 1% of that predicted by a well-established empirical correlation, $U_{T,\mathrm{Clift}} = 32.2$ cm/s (Clift et al. 2005, Eq. 7.3), and is also in good agreement with an experimental value of $U_{T,\mathrm{Houghton}} \approx 34$ cm/s (Houghton et al. 1957) considering the sensitivity of the rise velocity to the experimental conditions. Note that in the numerical work of Cano-Lozano et al. (2016) and the present work, surfactants are not modeled, and therefore these results correspond to pure water experimental conditions.

3.2. Turbulent bubbly flow validation

Having validated the DNS solver for a bubble rising in water, we now consider a vertical channel of liquid water that is initially at rest and randomly seed the flow with spherical air bubbles that are released from rest. Figure 2 shows a sketch of the vertical channel used for simulating the turbulent bubbly flow with gravity oriented in the negative y direction. The computational domain has dimensions of $20D_0 \times 40D_0 \times 20D_0$ in the x-, y-, and z-directions, respectively. Periodic boundary conditions are applied in the three spatial directions. The simulation is initialized by introducing spherical bubbles from rest with initial diameter $D_0 = 2$ mm in quiescent water. The void fraction of air bubbles is 0.5%, yielding an initial bubble count of 153; however, this number will decrease in time due to bubble-bubble coalescence. Table 1 summarizes the computational details, including the number of grid points in the horizontal direction $(N_x$ and N_z) and vertical direction (N_y) .

The bubbles are released at t=0, and the simulation is advanced in time until reaching

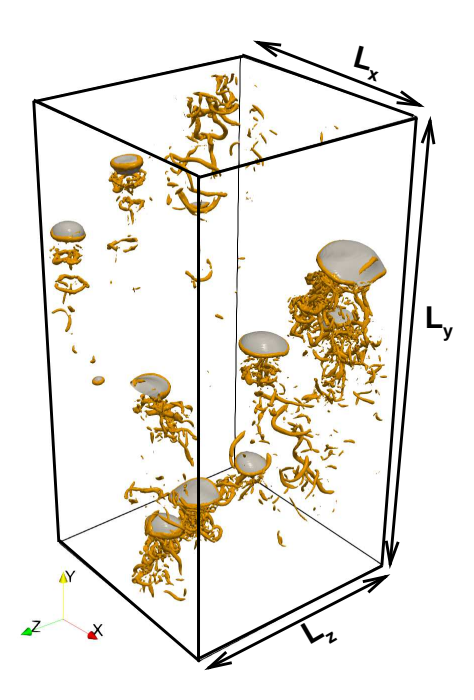


FIGURE 2. Instantaneous snapshot of the droplet interfaces (C=0.5) and vortical structures identified by Q isosurfaces.

Table 1. Computational setup and flow properties.

a quasi-steady state as marked by nearly constant values in time for the turbulent kinetic energy and its dissipation rate $(dk/dt \approx 0)$ and $d\varepsilon/dt \approx 0)$ at t=12 s, as shown in Figure 3. There is ongoing work to advance the simulations further in time such that a longer steady-state period can be achieved. When bubbles leave the top of the computational domain they re-enter the bottom of the domain using the same periodic mapping as used for the velocity and pressure. Considering the bubble's terminal velocity is $U_T \approx 30 \text{ cm s}^{-1}$, 12 seconds represent about 45 bubble flow-through times. The Taylor-scale Reynolds number based on the quasi-steady, spatially averaged values of k and ε in the liquid phase at the end of the simulation (t=12 s) is $Re_{\lambda} = 41.1$.

It is interesting to note the intermittent nature of the dissipation rate, $\varepsilon(t)$. The spikes in dissipation are due to bubble coalescence. When bubbles coalesce, there is a global reduction in surface area and therefore a reduction in interfacial surface energy. This excess surface energy is exchanged for turbulent kinetic energy through the power of the surface tension (Dodd & Ferrante 2016), leading to a jump in k(t) and a corresponding increase in $\varepsilon(t)$. At the final time, the number of bubbles has decreased from an initial

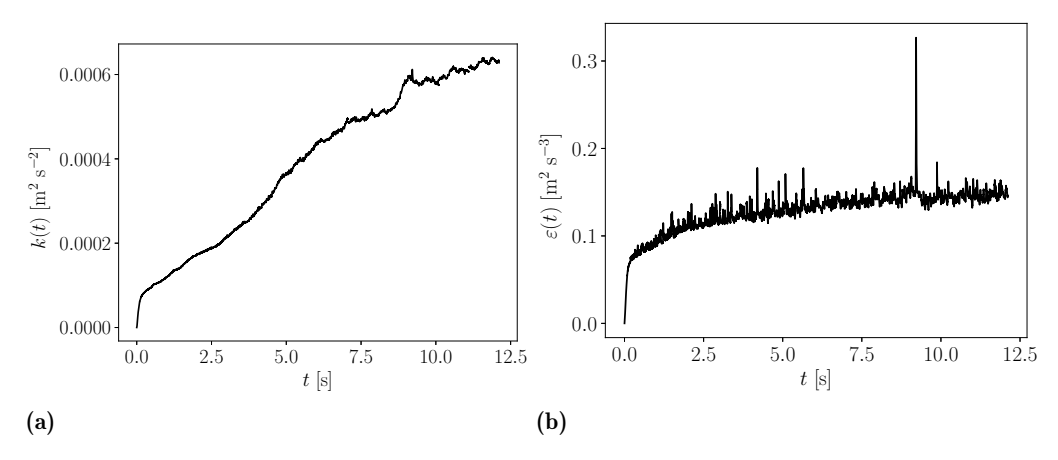


FIGURE 3. Time evolution of (a) turbulent kinetic energy and (b) its dissipation rate in the liquid phase.

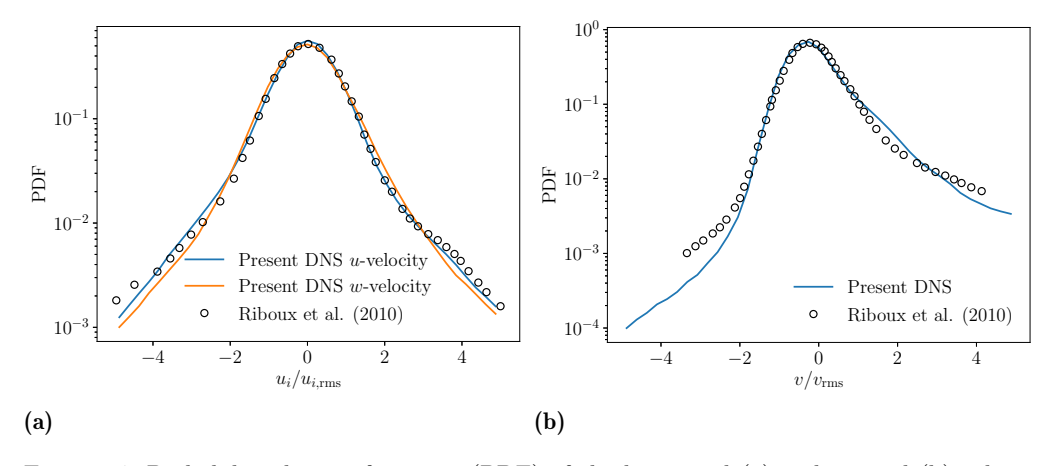


FIGURE 4. Probability density functions (PDF) of the horizontal (a) and vertical (b) velocity fluctuations normalized by their RMS value. The present DNS results are compared against the experimental results of Riboux *et al.* (2010).

value of 153 to about 10 due to coalescence. Figure 2 shows an instantaneous snapshot of the computational domain at t=12 s, which depicts the bubbles and vortical structures. To validate the DNS of bubble-induced turbulent flow, we compute the PDF of the velocity fluctuations in the horizontal and vertical directions and compare them to experimental values reported by Riboux et al. (2010). Figure 4 shows the PDF of the velocity fluctuations normalized by its RMS velocity comparing the present DNS results to the experiments which are for a void fraction of $\alpha=0.54\%$. Figure 4(a) shows the DNS is able to correctly capture the stretched exponential tails of the horizontal velocity (u and w) fluctuations and the PDF is symmetric about $u_i=0$, as expected. The vertical velocity (v) fluctuation PDF (Figure 4(b)) is skewed towards positive fluctuations in agreement with the experiment. Overall the agreement between the present DNS results and the experimental values is excellent.

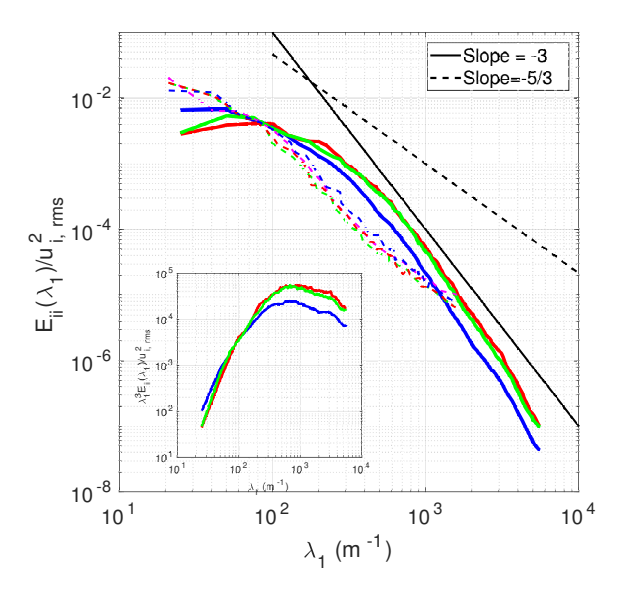


FIGURE 5. Energy spectra for the terminal stage. Solid lines are the current results and the dotted lines are the spectra from the experimental data extract. Different colors represent different velocity component as: $\operatorname{red} = u$ velocity, $\operatorname{green} = v$ velocity, $\operatorname{blue} = w$ velocity. The inset shows the compensated spectra in log-log scale.

Finally, we validate our DNS of bubbly turbulence for the turbulent kinetic energy spectra. As mentioned earlier, the experiment of Riboux et al. (2010) reported a -3 slope inertial subrange in their spectra. We only consider the liquid phase for the spectra. The computed energy spectra of all velocity components from the current simulation is plotted in Figure 5. The results from Riboux et al. (2010) are also added in the same plot. The horizontal axis of the spectra is the wavelength (λ_1) defined as $\lambda_1 = k/2\pi$, where k is the wavenumber. The vertical axis is normalized by the variance of velocity fluctuation. Indeed, our simulation, just as the experiments, also predicts a -3 power-law behavior in the spectra for all velocity components. This can be clearly seen in the inset of Figure 5, which shows the compensated energy spectra. These comparisons of spectra and PDF of velocity show that our simulation predicts several important features of bubbly flow reported in the literature.

4. Invariants of velocity gradient, strain- and rotation-rate tensors

Having discussed the validation of our DNS solver in the previous section, this section presents the analysis of small-scale turbulence. The invariants of velocity-gradient, strain-rate, and rotation-rate tensors are analyzed on various joint probability distribution function (JPDF) maps. The objective here is to look for the similarities and differences with respect to the single-phase HIT case. To this end, we also present plots from Ooi et al. (1999) with permission from the corresponding author of that paper. The results presented in this section are from the turbulent bubbly flow simulation.

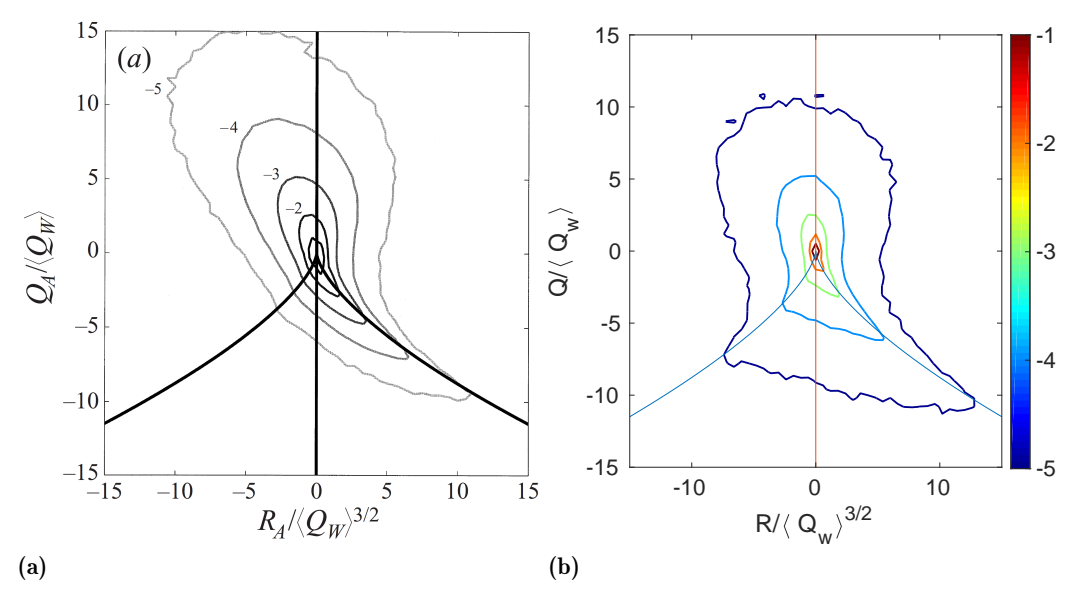


FIGURE 6. Joint PDF of Q and R obtained from (a) the HIT and (b) the current simulation. The blue line in (b) is the equation D=0 (refer to Eq. (1.4)). The isocontour levels in (a) and (b) are the exponents of probability. Plot (a) is used with permission from the corresponding author of Ooi *et al.* (1999).

$4.1. \ Q, R \ diagram$

We first present the JPDF between the second and third invariants of the VGT, which is commonly known as the Q, R diagram. The main purpose of the Q, R diagram is to reveal the relationship between the turbulent topology and vortex stretching/compression.

In order to understand the Q, R diagram, note that Q is the balance between enstrophy and strain-production. Therefore, positive Q represents the vorticity-dominated region, while the negative Q means the strain-dominated region.

The meaning of R depends on the sign of Q. For positive Q, R becomes $R \approx -(1/4)$ $\omega_i S_{ij} \omega_j$. This means that, for the vorticity-dominated regions, the positive R denotes vortex compression (i.e., destruction of enstrophy) and the negative R is for the enstrophy production by vortex stretching.

When Q < 0, $R \approx -(1/3)S_{ij}S_{jk}S_{ki} = -e_1e_2e_3$, where e_i , i = 1, 2, 3 are the strain-rate eigenvalues and they are called the extensive, intermediate, and compressive eigenvalues respectively. For the HIT, the extensive (e_1) and the compressive (e_3) strain-rate eigenvalues are always positive and negative, respectively. The intermediate strain-rate eigenvalue (e_2) can be either negative or positive. The sign of e_2 determines the geometry of strain-dominated regions. If e_2 is positive, then we have two stretching directions and one compressive direction, which represent a sheet-like strain-dominated structure. On the other hand, a negative e_2 yields a tube-like strain-dominated structure with two compressive and one stretching directions. Therefore, a positive R represents a sheet-like and a negative R means a tube-like straining structure.

We have computed the normalized mean values of Q and R and found their values as $\langle Q \rangle / \langle S_{ij} S_{ij} \rangle = -0.0574$ and $\langle R \rangle / \langle S_{ij} S_{ij} \rangle^{3/2} = 0.0271$. Note that these normalized values become zero when we include all the mesh points, including the points that lie

inside the bubble. The nonzero values obtained for the liquid phase suggest that the bubbly turbulence is inhomogeneous in small scales. They also indicate that the flow, on average, is more strain-dominated.

The Q,R diagram is widely reported in the literature for various cases (Chong et al. 1990; Blackburn et al. 1996; Gomes-Fernandes et al. 2014; Paul et al. 2017). These cases vary from mixing layers, boundary layers, jets, wakes, and triply periodic HIT. The Q,R diagram has a universal tear-drop shape with higher correlation in two regions: Q>0 with R<0 that resembles enstrophy production in vorticity-dominated regions, and Q<0 with R>0 meaning sheet-like structures of strain-dominated regions (Tsinober 2009).

The typical Q,R diagram reported in the literature is shown in Figure 6(a). This plot is adopted from Ooi et al. (1999) for a forced HIT at $Re_{\lambda}=70.9$. The result from the current simulation is plotted in Figure 6(b). The similarity between these two plots is found in the strain-dominated regions (i.e., Q<0). Here, the production of strain is more preferred than the enstrophy production. Besides, the geometry of the strain-dominated region is of sheet-like in nature. However, a significant difference is noted in the vorticity-dominated region, where the preference for vortex stretching is not properly defined for the current case. In vorticity-dominated regions of bubbly turbulence, there seems to be an equal tendency to produce velocity gradients of strain (R>0) and of vorticity (R<0), while the classical result has a clearly defined preference for enstrophy production through vortex stretching. This is the first evidence that the VGT dynamics of bubbly turbulence is not similar to that of the HIT. It is interesting that we observe a clearly defined -3 slope where the vortex stretching is not properly defined.

4.2.
$$Q_s, R_s$$
 diagram

While the Q,R diagram helps us to understand some features of flow topology, the Q_s,R_s diagram provides more information about the nature of the straining process and its associated geometry. In turbulent flows, Q_s is always negative. Therefore, the topology information from the Q_s,R_s diagram depends on the sign of R_s . As we noted previously, $R_s=-e_1e_2e_3$. Therefore, $R_s>0$ resembles the strain-dominated regions with sheet-like structures, while $R_s<0$ the tube-like strain-dominated region. More information about the nature of straining can be obtained by writing R_s in terms of the strain-rate eigenvalues ratios. If $a=e_2/e_1$, then R_s can be written as

$$R_s = (Q_s)^{3/2} a (1+a) (1+a+a^2)^{3/2}$$
(4.1)

The nature of the straining is given in terms of the strain-rate eigenvalues ratios. If a=0, then the ratio $e_1:e_2:e_3$ is 1:0:-1 which corresponds to two-dimensional flow. Likewise, a=1 yields 1:1:-2 which denotes axial stretching. Similarly, a=-1/2 gives 2:-1:-1 that stands for axial contraction. Finally, for a=1/3, we get the ratio as 3:1:-4, meaning the straining is of bi-axial stretching.

The Q_s, R_s diagram from the literature is given in Figure 7(a). The diagram is clearly skewed toward positive R_s , leading to the conclusions made from the Q, R diagram that the strain-dominated regions are statistically sheet-like in nature. Furthermore, Figure 7(a) also shows that the higher probability values are along the line $e_1:e_2:e_3=1:1:-2$, which corresponds to axial stretching. The Q_s, R_s diagram of a bubbly flow is depicted in Figure 7(b). The plot is qualitatively similar to that of the literature result. The only minor difference is that the more probability in this JPDF is found to be along the line $e_1:e_2:e_3=3:1:-4$, resembling bi-axial stretching. However, the strain-rate eigenvalues

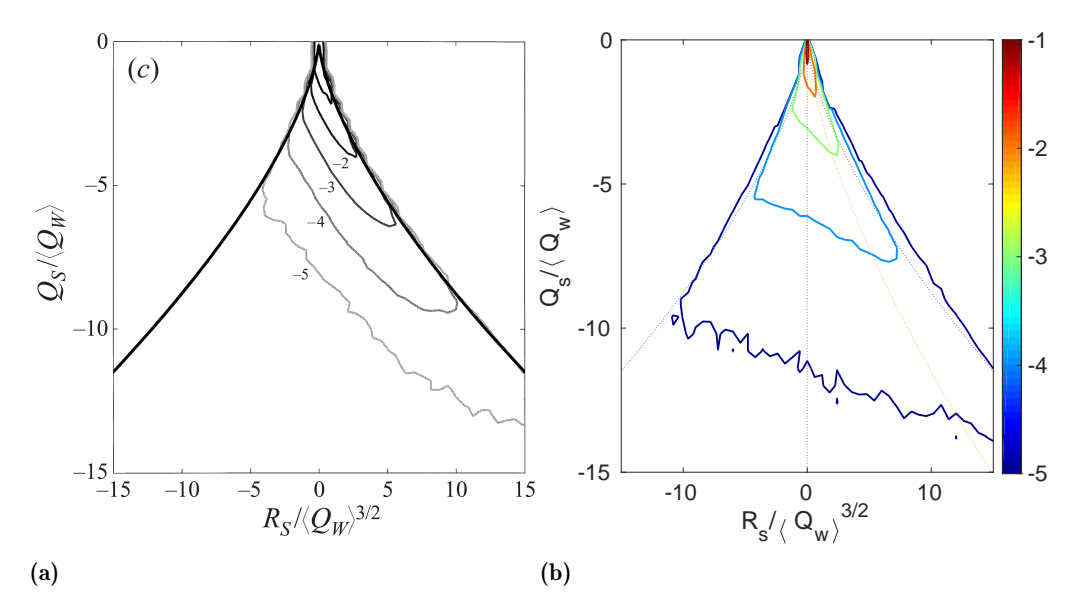


FIGURE 7. Joint PDF of Q_s and R_s obtained from (a) the HIT and (b) the current simulation. The lines in (b) correspond to different strain-rate eigenvalues ratios. From left to right, they correspond to $e_1: e_2: e_3 = 2:-1:-1$, 1:0:-1, 3:1:,-4, and 1:1:-2. The isocontour levels in (a) and (b) are the exponents of probability. Plot (a) is used with permission from the corresponding author of Ooi $et\ al.\ (1999)$.

are generally found to be between 1:1:-2 and 3:1:-4 for various flow configurations (da Silva & Pereira 2008; Gomes-Fernandes *et al.* 2014). Therefore, the Q_s, R_S diagram does not exhibit anything substantially different from the classical result. In bubbly turbulence, as in the HIT, the strain-dominated regions are generated by bi-axial stretching and are statistically sheet-like in nature.

4.3.
$$-Q_s, Q_w$$
 diagram

The final JPDF map widely used in the study of small-scale turbulence is the $-Q_s, Q_w$ diagram. The main purpose of this diagram is to understand the topology of the dissipative and vortical regions. Since $-Q_s$ and Q_w are always positive, the interpretation of this diagram depends on the direction along which the JPDF contours are aligned. In this diagram, the horizontal axis represents structures with higher values of enstrophy with little dissipation (i.e., vortex tubes). The vertical axis belongs to irrotational dissipation with a high amount of strain and with little or no vorticity. A 45^o line (i.e., $-Q_s = Q_w$ line) marks the structures with a high amount of strain and vorticity which is equivalent to a vortex sheet.

The normalized value of $\langle Q_w \rangle / \langle -Q_s \rangle$ should be 1.0 for HIT. In our case, this value is found to be 0.8859. This difference shows that the bubbly flow is inhomogeneous and it is, on average, dominated by strain. Similar values were also reported in other studies (Gomes-Fernandes *et al.* 2014; Paul *et al.* 2017).

The $-Q_s$, Q_w diagram from the literature is given in Figure 8(a). The behavior of the $-Q_s$, Q_w diagram is found to be dependent on the flow. For example, in Figure 8(a), which is plotted for the forced HIT, every self-similar JPDF contour has a maximum of Q_w , which is almost twice that of $-Q_s$ revealing an equal probability for vortex sheets

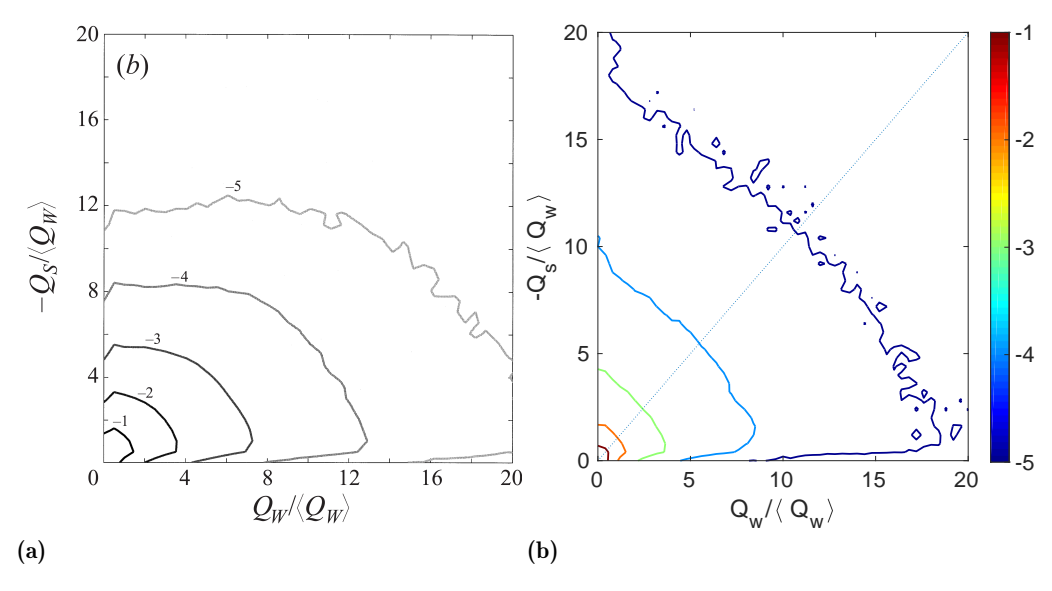


FIGURE 8. Joint PDF of $-Q_s$ and Q_w obtained from (a) the HIT and (b) the current simulation. The dashed blue line in (b) corresponds to the $-Q_s = Q_w$ equation. The isocontour levels in (a) and (b) are the exponents of probability. Plot (a) is used with permission from the corresponding author of Ooi *et al.* (1999).

and tubes with higher magnitude of enstrophy. Interestingly, studies on grid turbulence reported $-Q_s$, Q_w diagrams that are approximately symmetric about the 45^o line, with the maximum of $-Q_s$ for every contour that is similar to that of Q_w . The $-Q_s$, Q_w diagram of the current simulation is shown in Figure 8(b). In bubbly flows, we note that the contours of $-Q_s$, Q_w are more aligned toward the vertical axis, with the maximum value of $-Q_s$ for every contour that is more than that of $-Q_w$. This is the opposite of what is observed for the HIT. The bubbly flows thus seem to be dominated by strain with the structures of vortex sheets and vortex tubes.

5. Conclusions

We have analyzed the DNS data of turbulent flow due to rising bubbles. Our work had two objectives: to provide validation of the solver and to understand the similarities and differences in small-scale invariants between the HIT and bubbly turbulence.

The DNS solver was validated for an air bubble rising in quiescent water. The time evolution of the bubble Reynolds number was in good agreement with computational data by Cano-Lozano et al. (2016). Additionally, the final velocity of the bubble was within 1% of that predicted by an experimentally validated empirical correlation. Next, the solver was validated for bubble-induced homogeneous turbulence for a void fraction of 0.5%. We computed the PDFs of the horizontal and vertical velocity fluctuations and compared them with those computed from those reported in the literature. The DNS results are in excellent agreement with the experimental data of Riboux et al. (2010).

To analyze the small-scale turbulence, we considered three different JPDFs from the invariants of the velocity-gradient, strain-rate, and rotation-rate tensors. They are (i) Q, R, (ii) $Q_s, R_S,$ and (iii) $-Q_s, Q_w$ diagrams. Out of these three, only the Q_s, R_s diagram

is similar to that of the HIT. Some significant differences are noted in the other two diagrams. The Q,R diagram of bubbly flow does not attain its regular tear-drop shape even in the terminal stage of the simulation. This is because of a less-defined correlation for Q>0 and R<0. As a result, the bubbly flow is statistically strain-dominated, while the preference for vortex stretching over vortex compression is not as well defined as in the HIT. The Q_s, R_s diagram reveals that the highly-dissipative regions in the bubbly flow are statistically sheet-like in nature, and they are generated mostly by bi-axial stretching. Finally, while the contours of the $-Q_s, Q_w$ diagram for the HIT are aligned toward the vortex tube axis, the bubbly flow $-Q_s, Q_w$ diagram contours are clearly aligned toward the irrotational dissipation axis. The maximum of $-Q_s$ is more than that of Q_w in the bubbly flows, whereas the reverse is reported for the HIT. Moreover, vortex sheets and vortex tubes are highly preferred both in bubbly flows and in the HIT.

Acknowledgments

The authors are thankful to Prof. Julio Soria of Monash University for kindly allowing the use of plots from Ooi *et al.* (1999). This work was supported by the Office of Naval Research (ONR), Grant No. N00014-15-1-2726.

REFERENCES

- Baraldi, A., Dodd, M. S. & Ferrante, A. 2014 A mass-conserving volume-of-fluid method: volume tracking and droplet surface-tension in incompressible isotropic turbulence. *Comput. Fluids* **96**, 322–337.
- Blackburn, H., Mansour, N. & Cantwell, B. 1996 Topology of fine-scale motions in turbulent channel flow. *J. Fluid Mech.* **310**, 269–292.
- Cano-Lozano, J. C., Martinez-Bazan, C., Magnaudet, J. & Tchoufag, J. 2016 Paths and wakes of deformable nearly spheroidal rising bubbles close to the transition to path instability. *Phys. Fluids* 1, 053604.
- Chong, M., Perry, A. & Cantwell, B. 1990 A general classification of three-dimensional flow fields. *Phys. Fluids* 2, 765–777.
- CLIFT, R., GRACE, J. R. & WEBER, M. E. 2005 Bubbles, Drops, and Particles. Courier Corporation.
- Dodd, M. S. & Ferrante, A. 2014 A fast pressure-correction method for incompressible two-fluid flows. *J. Comput. Phys.* **273**, 416–434.
- Dodd, M. S. & Ferrante, A. 2016 On the interaction of Taylor lengthscale size droplets and isotropic turbulence. *J. Fluid Mech.* **806**, 356–412.
- Gomes-Fernandes, R., Ganapathisubramani, B. & Vassilicos, J. 2014 Evolution of the velocity-gradient tensor in a spatially developing turbulent flow. *J. Fluid Mech.* **756**, 252–292.
- HOUGHTON, G., RITCHIE, P. & THOMSON, J. 1957 Velocity of rise of air bubbles in sea-water, and their types of motion. *Chem. Engr. Sci.* 7, 111–112.
- Kolmogorov, A. 1941 The local structure of turbulence in incompressible viscous fluid for very large Reynolds numbers. In *Dokl. Akad. Nauk SSSR*, , vol. 30, pp. 299–303.
- MENEVEAU, C. 2011 Lagrangian dynamics and models of the velocity gradient tensor in turbulent flows. *Annu. Rev. Fluid Mech.* **815**, 219–245.
- Ooi, A., Martin, J., Soria, J. & Chong, M. 1999 A study of the evolution and char-

- acteristics of the invariants of the velocity-gradient tensor in isotropic turbulence. J. Fluid Mech. 381, 141–174.
- Paul, I., Papadakis, G. & Vassilicos, J. 2017 Genesis and evolution of velocity gradients in near-field spatially developing turbulence. J. Fluid Mech. 815, 295–332.
- RIBOUX, G., RISSO, F. & LEGENDRE, D. 2010 Experimental characterization of the agitation generated by bubbles rising at high Reynolds number. *J. Fluid Mech.* **643**, 509–539.
- RICHARDSON, L. 1926 Atmospheric diffusion shown on a distance-neighbour graph. Proc. R. Soc. Lond. A pp. 709–737.
- DA SILVA, C. & PEREIRA, J. 2008 Invariants of the velocity-gradient, rate-of-strain, and rate-of-rotation tensors across the turbulent/nonturbulent interface in jets. *Phys. Fluids* **20**, 055101.
- SREENIVASAN, K. & ANTONIA, R. 1997 The phenomenology of small-scale turbulence. *Annu. Rev. Fluid Mech.* **29**, 435–472.
- TSINOBER, A. 2009 An Informal Conceptual Introduction to Turbulence. Springer.